Embedding a Water Vapor Radiometer in a DSN Antenna: Experimental Results From DSS 13

A. B. Tanner[1]

Brightness temperature measurements at 22.2 GHz, 23.8 GHz, and 31.4 GHz collected by a water vapor radiometer (WVR) embedded within the DSS-13 beam-waveguide (BWG) optics are presented and compared with simultaneous measurements from an identical reference radiometer located outside of the beam waveguide. The objective of these tests is to assess the feasibility of measuring tropospheric water vapor with an embedded microwave radiometer. Such a system potentially could reduce path-delay estimation errors associated with the antenna offset and beam mismatch of the current stand-alone WVR.

The data show that the excess noise temperature of the BWG antenna is considerable—on the order of 6 to 12 K—and that the noise temperature varies greatly depending on azimuth and elevation positions, feedhorn gain and alignment, and ambient temperature. The data also show that the excess noise of the BWG is a very smooth function of these variables. For time scales of up to 300 seconds and spatial scales up to about 30 degrees, the excess noise during individual azimuth scans of the antenna while at a 20 degree elevation angle can be fit to within 0.03 K with a radiative transfer model that involves a three-harmonic Fourier expansion versus azimuth. Above 45 degrees of elevation angle, the excess noise can be fit to about 0.01 K for the same spatial and temporal scales. Side-lobe contamination is believed to determine these error levels. At longer time scales (3 days at a fixed zenith position), fits versus ambient temperature and surface humidity show residual errors on the order of 0.1 K. At short time scales of less than ∼300 seconds, the difference between the embedded and the external measurements are shown to be dominated by the atmospheric variability and sampling differences associated with antenna pattern mismatch and the spatial offset between the two systems. These results indicate that an embedded radiometer operating in conjunction with an external radiometer would offer significant advantages over the stand-alone external radiometer on short time scales. Such measurements would fill a gap in present tropospheric path-delay calibration capabilities for time scales of less than 300 seconds.

---

[1] Microwave and Lidar Technology Section.

The research described in this publication was carried out by the Jet Propulsion Laboratory, California Institute of Technology, under a contract with the National Aeronautics and Space Administration.

I. Introduction

Water vapor in the Earth's atmosphere slows the propagation of radio signals and is a source of error for radio science experiments in which precise path delays (or high phase stability) through the atmosphere are required. Water vapor radiometers provide a means of measuring this path delay along a given line of sight by observing the thermal emissions of water vapor near a resonance at 22.2 GHz [6]. At the DSN, the upcoming series of Cassini gravitational wave experiments (GWE) will require the most precise measurements of atmospheric path delay possible. Two radiometers, dubbed the advanced water vapor radiometers (AWVRs), have been built specifically to support the GWE [2]. For the past year, these two radiometers have been operating at DSS 15 and at DS 13, respectively, during a series of validation tests [1]. The AWVRs observe the sky brightness temperature at frequencies of 22.2 GHz, 23.8 GHz, and 31.4 GHz.

One compromise in the design of the AWVRs is that they do not sample the same atmospheric volume as the DSN antenna. Each AWVR normally operates outside and adjacent to the DSN antenna on an independent antenna and positioning system. There are practical reasons for separating the AWVR in this way—including the need to perform tip-curve calibrations and to control antenna losses and side lobes—but the consequence is that the antenna pattern of the DSN antenna does not precisely match that of the AWVR. The AWVRs are offset approximately 40 meters to the south of the DSS-25 or DSS-13 beam-waveguide antennas, and they view the atmosphere in a 1 degree conical antenna beam that is mismatched to the 34-meter-diameter column in the near field of the BWG antennas. In the presence of small-scale water-vapor structure, this mismatch and offset results in path-delay estimation errors that are significant on 10 to 300 second time scales. The major requirements for Cassini GWE occur at longer time scales of 1,000 to 10,000 seconds and will be met with the current system. However, there are a variety of applications, such as gravity field mapping during a planetary fly-by, in which 100 second time scales are a concern [3,7]. For these experiments, a WVR may need to be embedded in the optics of the DSN antenna. To assess the feasibility of such a measurement, the noise temperature of the BWG needs to be well characterized.

In this article, we present data collected in March of 2000 using the serial number 1 AWVR (or the A-1 radiometer) located just to the south of the DSS-13 beam-waveguide antenna and the serial number 2 AWVR (A-2), which was placed at the F-3 focal point of the DSS-13 beam-waveguide optics in the pedestal room. Figure 1 depicts the layout of the experiment. The antenna feedhorn of the AWVR is built into the radiometer enclosure and is reasonably compatible with the beam-waveguide optics. This made the experiment very simple to perform. Moreover, because of the long-term stability of these radiometers, there was no need to recalibrate the AWVR while it was in the beam waveguide (e.g., as with a liquid nitrogen target). Tip-curve calibrations performed before and after the BWG experiments show very little change. The high confidence in the absolute calibration of the A-2 radiometer together with the reference data provided by the A-1 radiometer provided a unique opportunity to accurately characterize the differences of the two systems.

II. Alignment and Calibration

Alignment of the AWVR within the BWG pedestal room was based on drawings[2] that established the desired focus position and feedhorn gain for the maximum gain-versus-system noise temperature ratio, or G/T. For the DSS-13 BWG, a feedhorn gain near 25.5 to 25.8 dB is considered optimal. Table 1 summarizes the operating frequencies and feedhorn gains of the AWVR. The AWVR feedhorn provides a very nearly Gaussian and rotationally symmetric antenna pattern. Note that only the 31.4 GHz channel of the AWVR has the "optimum" gain for the BWG.

[2] Provided by W. Veruttipong, personal communications, Jet Propulsion Laboratory, Pasadena, California, 2000.

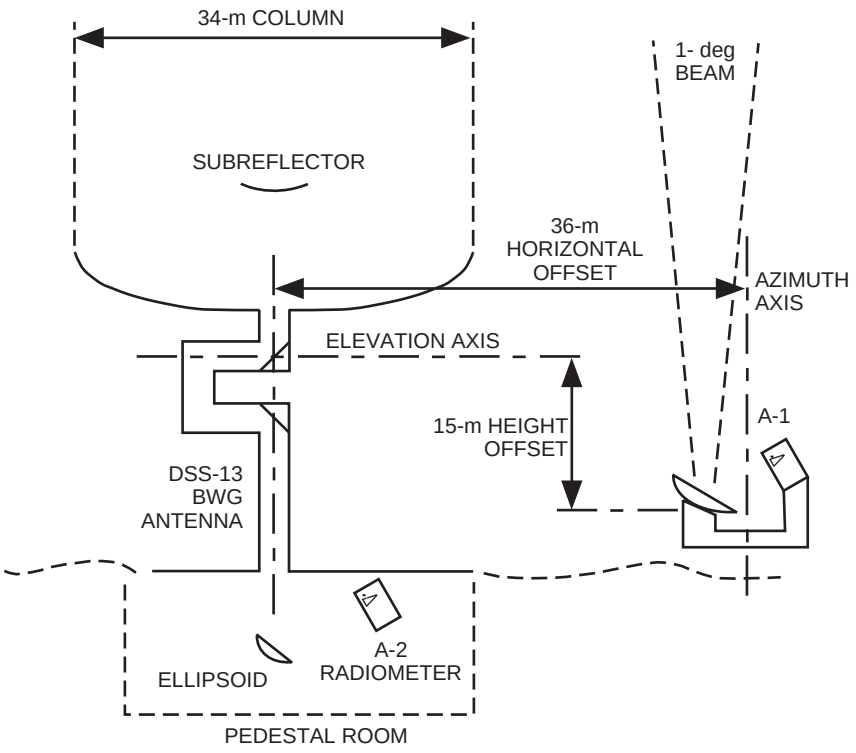

Fig. 1. Layout of the embedded AWVR experiment (not to scale).

Table 1. AWVR operating frequencies and feedhorn gain.

Frequency, GHz	Feedhorn gain, dB
31.4	25.7
22.2	22.6
23.8	23.4

The AWVR was mounted to the ceiling of the pedestal room at DSS 13 at a downward inclination of 30 degrees such that the feedhorn pointed at the ellipsoid in the center of the pedestal room, as shown in Fig. 1. The initial alignment of the ceiling fixture was based on a tape-measured radius from the BWG center axis and a tape-measured drop from the ceiling. The final alignment involved the use of a borescope mounted in the center of the BWG ellipsoid to site the AWVR feedhorn along the optical axis of the BWG and then a tape measurement to set the focus position. The ellipsoid positioner of the BWG was rotated about the beam waveguide's center axis to align the borescope with the feedhorn in the side-to-side direction, and the vertical offset was adjusted by moving the radiometer on its mount. The focus was set according to drawings such that the distance between the ellipsoid center (i.e., the intersection of the BWG center axis and the ellipsoid surface) and the phase center of the AWVR feedhorn was 167.8 inches (426.2 centimeters). Using a tape measure and a plumb bob, the radius from the BWG center axis to the phase center of the feedhorn and the height of the feedhorn above the pedestal room floor were remeasured. All dimensions agreed with the drawings to within 0.1 inches (0.25 centimeters).

Figure 2 gives measured excess noise as the ellipsoid was rotated on the center axis of the BWG for alignment purposes. The horizontal scale is the indicated ellipsoid positioner angle (referenced to north), and the vertical scale is the brightness temperatures of the A-2 radiometer minus the brightness temperatures of the A-1 radiometer at the three observing frequencies. The BWG antenna and the A-1 radiometer were both pointed at zenith. Aside from the different noise temperatures among the different frequencies—which presumably are related to the feedhorn gain—Fig. 2 shows a broad minimum between 112.4 degrees and 113.0 degrees. This range of angles translates to 1.5 inches (3.8 centimeters) at the focal point. Such a wide tolerance was fortunate since—owing to an error in note keeping—most of the measurements were conducted with an ellipsoid setting of 113.0 degrees when the correct setting should have been 112.7 degrees based on the borescope alignment. This error was caught only late in the experiment. Fortunately, subsequent analysis showed this error to be largely inconsequential.

Figure 3 gives excess noise-versus-focus position. These data were collected as the AWVR was moved along the 30 degree incline either toward (negative displacement in Fig. 3) or away from the ellipsoid center. The ellipsoid position was fixed at 112.7 degrees, and both antennas were pointed at zenith. Evidently, the lowest noise is beyond this plot at a focus position less than 163.8 inches (416 centimeters), $(426 - 10$ centimeters). One possible explanation for this is that feedhorn spillover past the edges of the ellipsoid are reduced by bringing the feed close to the ellipsoid. Figure 3 does not in any way indicate antenna gain, however, and one should be careful to note that these data do not indicate where the best focus position is for the optimum G/T ratio.

The calibrations for both the A-1 and A-2 radiometers were based on tip-curve procedures performed before and after the A-2 radiometer was in the DSS-13 BWG. The tip-curve procedure is a common calibration technique used to remove the atmospheric contribution from clear-sky observations so that the cosmic background temperature of 2.7 K can be utilized as a cold-temperature reference [6]. The procedure involves repeatedly tipping the radiometer's viewing angle between zenith and the horizon until a regression fit of output voltage against the known air mass (equal to the cosecant of the elevation angle) yields sufficient accuracy. On dry days, the tip-curve procedure yields calibrations accurate to within 0.1 K, but typically it can take several days of continuous tipping before variability in the atmosphere can be averaged down to the 0.1 K level.

Figure 4 summarizes the results of tip-curve calibrations performed on the A-2 radiometer at the DSS-15 site in the months before and after the beam-waveguide experiment. An average of these data

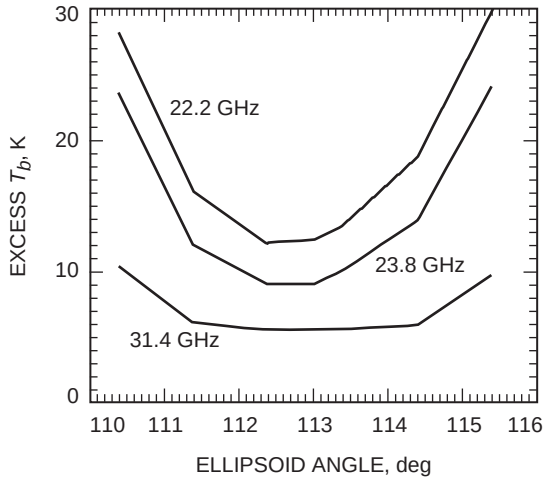

Fig. 2. Brightness temperature difference (A-2 minus A-1 brightness temperature) as a function of ellipsoid position.

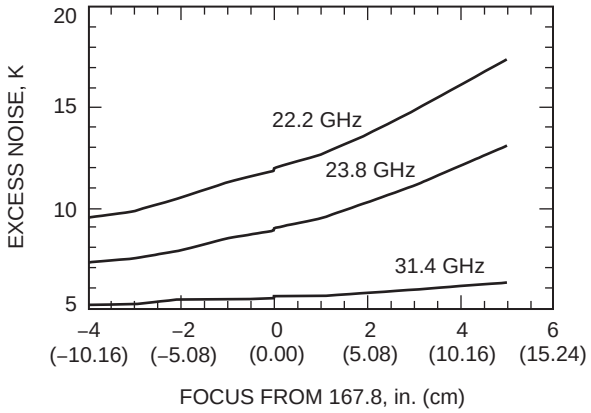

Fig. 3. Brightness temperature difference (A-2 minus A-1 brightness temperature) as a function of focus position as measured in the distance between the ellipsoid center and the phase center of the AWVR feedhorn.

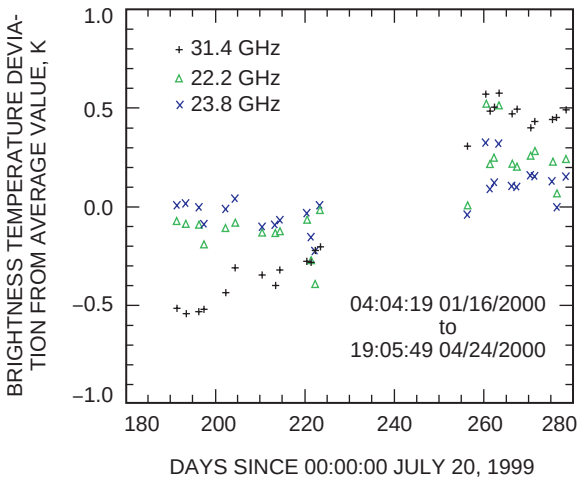

Fig. 4. Calibration history of serial no. 2 AWVR based on tip-curve analysis before and after the BWG experiment.

was used during the beam-waveguide experiment, and the large gap in the middle of this time series corresponds to the month that the A-2 radiometer was placed in the DSS-13 beam waveguide. Most of the scatter in Fig. 4 is due to limitations of the tip-curve procedure in the presence of atmospheric water-vapor variability. This is evident in the fact that the channels that are more sensitive to water vapor (22.2 and 23.8 GHz) exhibit proportionally greater scatter. Only the long-term drift of about 1 K evident in the 31.4 GHz channel in 60 days is believed to be a real instrumental error. From these data, the estimated absolute brightness temperature error in the 31.4 GHz channel is approximately ±0.2 K during the 30 days of the BWG experiment. The 22.2 and 23.8 GHz errors are on the order of ±0.1 K for the same period.

Another error to note is the losses in the A-2 radiometer's offset parabola, which are present during the tip-curve procedures but not in the BWG. Reflector loss estimates are factored out of the BWG data presented below. The reflector presents 0.5 to 0.9 K of noise, depending on frequency, and confidence in the loss estimates is about ±0.05 K.

Outside of the BWG, the A-1 radiometer exhibited better stability (not plotted here for brevity). The A-1 radiometer also performed tip-curves throughout the BWG experiment, which further improved the calibration confidence. The estimated errors in A-1 are ±0.1 K in absolute brightness temperature at all frequencies. Combined, the absolute errors in the measured difference of the A-1 radiometer and the A-2 radiometer brightness temperature during the BWG experiments are approximately ±0.2 K in the 22.2 and 23.8 GHz channel and ±0.3 K in the 31.4 GHz channel.

III. Observations

Table 2 catalogs the BWG experiments performed in March of 2000. The majority of the observation time was at zenith while the BWG antenna was parked and unattended in the stow position (at an azimuth of 140 degrees and an elevation of 90 degrees). All other antenna positions required attendance by DSN personnel. Most of these attended observations were either at a fixed position in both azimuth and elevation or at a fixed elevation while the azimuths of the two antennas were slowly scanned in unison. The fixed elevation-angle data were preferred for ease of analysis. Only one data set, on March 24, 2000, was collected in a sidereal tracking mode (i.e., with motion in both azimuth and elevation).

The best data set of Table 2 lasted 3 days, starting on March 17 at 1600 UT (8 A.M. local time). The following discussion and analysis will initially concentrate on this time series because it was free of clouds,

Table 2. Summary of BWG experiments performed in March 2000.

Date	UT	Duration	Notes
3/01/00	2300	∼1 h	Initial installation, zenith as ellipsoid adjusted and set to 113.0 degrees
3/02/00	2400	9 h	Zenith, cloudy, rain
3/09/00	1600	4 h	Fixed at azimuth/elevation = 180/20 degrees
3/10/00	1715	6.5 h	Fixed at azimuth/elevation = 180/20 degrees
3/10/00	2400	2.6 days	Zenith
3/16/00	1600	4 h	0.1 degree/second azimuth scans at 20 and 90 degrees, interrupted
3/17/00	1600	8 h	0.05 degree/second azimuth scans at 20, 90, and 45 degree elevation
3/17/00	2400	2.6 days	Zenith
3/23/00	1600	4 h	0.1 degree/second azimuth scans at 20 and 45 degree elevation, ellipsoid moved to 112.7 degrees from 113.0, cloudy
3/24/00	1600	8 h	Sidereal track, restart at 18.7 h UT to avoid sun
3/24/00	2400	1.6 days	Zenith
3/27/00	1620	30 min	Zenith as focus is adjusted, elipsoid = 112.7 degrees azimuth
3/27/00	1700		Removed A-2 from BWG

all hardware and software worked well, and the data set covered a wide span of temperature, humidity, and antenna positions.

BWG observations were recorded from the morning of Friday, March 17, 2000, until the following Monday morning. Figure 5 gives the brightness temperature observed in the 23.8 GHz channels of both A-1 and A-2 during this time. The time scale of this plot is UT days with UT day 2.0 = 4 P.M. PST on Friday. At the start of this time series, and during the day on Friday, the DSS-13 antenna was commanded to make three slow scans in azimuth at fixed elevations of 20 degrees, 90 degrees (zenith), and 45 degrees, respectively. This sequence is evident in the stepped brightness temperatures prior to day 2.0 of Fig. 5. From day 2.0 to day 4.5, the antenna was parked at zenith with an azimuth of 140 degrees.

Temperature and humidity from surface metrology outside of DSS 13, along with temperature within the pedestal room of DSS 13, are summarized in Fig. 6. Figure 6 also includes a derived estimate of an effective temperature, T_S, plotted in red, to be used with noise temperature calculations. The details of this derived temperature are discussed below.

Figure 7 gives the difference of the A-1 and A-2 brightness temperatures at all three of the observing frequencies. This temperature difference is excess noise added by the BWG. Again, the large disparity of excess noise among the three frequencies is believed to be related to the feedhorn gain. Otherwise, the time series from 2.0 to 4.5 days shows a distinct diurnal variation that apparently correlates with outside air temperature (see Fig. 6).

Figure 8 gives the same data as Fig. 7 for an expanded time series during the azimuth scans. Figure 9 gives the azimuth position of the BWG for the same period. The A-1 radiometer scanned together with the BWG to an accuracy of about 0.1 degree. The interruption—or transient—near 1.82 days was caused by a software error at 90 degrees of elevation (pointing the BWG to 89.999 degrees avoids this problem). Note that for the three azimuth scans in Fig. 9 the scan rate was 0.05 degrees/second, and the azimuth

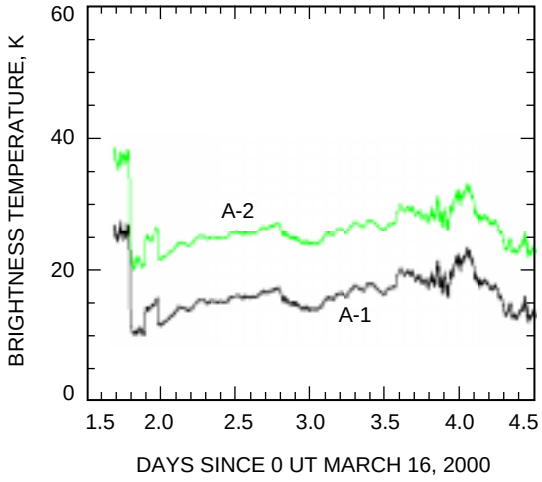

Fig. 5. Brightness temperature at 23.8 GHz of the A-1 outside the DSS-13 BWG and the A-2 in the BWG. Days 1.6 to 2.0 were recorded during azimuth scan, 2.0 to 4.5 at zenith.

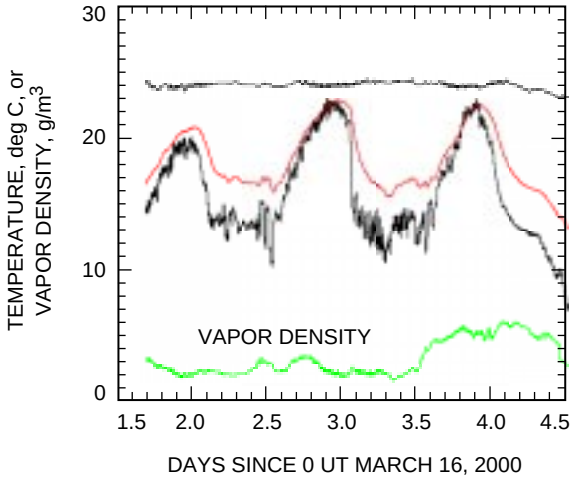

Fig. 6. Vapor density (green) and temperature (second from bottom) from surface metrology; ambient temperature within the BWG (top) and estimated effective temperature (red), T_S, for analysis.

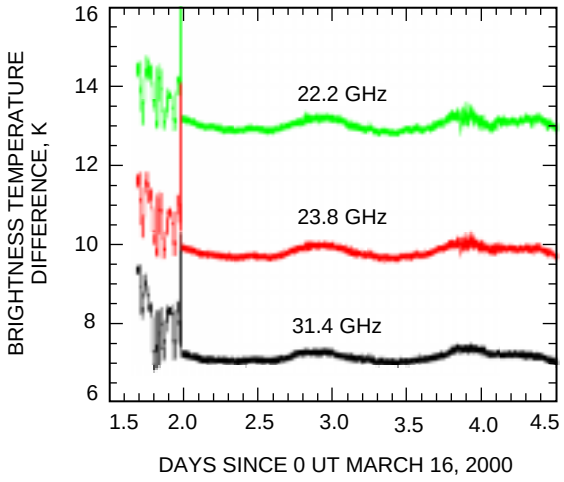

Fig. 7. Brightness temperature difference: A-2 T_B — A-1 T_B.

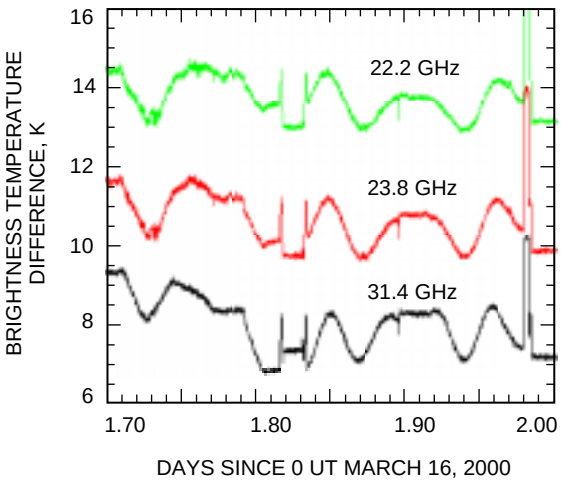

Fig. 8. Expansion of scale from day 1.7 to day 2.0 to show variations during azimuth scans.

range was 10 degrees to 290 degrees. The A-1 radiometer is blocked by the DSS-13 antenna outside this range. The variations of Fig. 8 are clearly related to the antenna position in Fig. 9.

IV. Analysis

A. Fitting and Removing the Effects of BWG Losses

To model the above errors, the following analysis will treat the BWG as a lumped-element loss so that a simple radiative transfer equation can be used to predict the brightness temperature of A-2 within the BWG from the brightness temperature observed by the A-1 radiometer outside of the BWG:

$$T_{B2} \simeq (1 - L)T_{B1} + LT_S \tag{1}$$

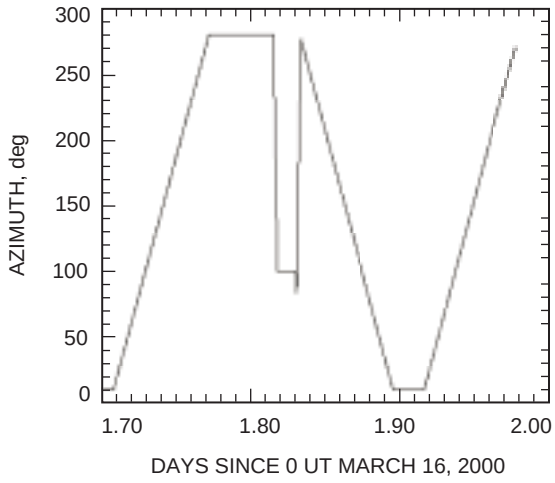

Fig. 9. Azimuth of the BWG antenna for comparison with Fig. 8. Elevation (not shown) started at 20 deg, moved to 90 deg at 1.8 days, and then moved back down to 45 deg at 1.9 days.

where T_{B2} and T_{B1} are brightness temperatures seen by A-2 and A-1, respectively; L is the lumped-element loss of the beam-waveguide antenna; and T_S is the effective temperature of this lumped-element loss.

The loss term in Eq. (1), L, incorporates all losses that prevent the radiometer from seeing the sky. This includes both ohmic and scattered losses within the BWG, ground pickup by scattered losses (e.g., antenna side lobes caused by quadripod scatter), and absorption by the air and water vapor within the BWG. The relative magnitudes of these elements is not yet known, but the net loss can be estimated from the present data set given an estimate of T_S. The estimated "effective" temperature, T_S, is a weighted average of temperatures throughout the BWG. The closest available measurements for estimating T_S are outside air temperature and pedestal room air temperature, as plotted in Fig. 6. The red trace plotted in Fig. 6 represents a best effort to mix these two air temperatures to form an estimate of T_S. Based on a fit to the diurnal variations of Fig. 7, T_S is approximately equal to 0.7 times the outside air temperature plus 0.3 times the pedestal room air temperature. A low-pass filter with a 1.5 hour time constant was applied to simulate the thermal inertia of the BWG.

From Figs. 8 and 9, the BWG loss appears to be a smooth and almost sinusoidal function of azimuth positions, which suggests that the azimuth dependence may be represented as a Fourier series. With some experimentation, the following three-harmonic expansion for a lumped-element BWG loss versus azimuth has been found to provide a good fit when applied to individual azimuth scans at a given elevation and RF frequency:

$$L_m = d_v v_d + a_{0m} + \sum_{n=1}^{n=3} \left[a_{nm} \cos(n * az) + b_{nm} \sin(n * az) \right] \tag{2}$$

where the subscript m denotes a particular elevation angle and the term $c_v v_d$ is added to account for the water-vapor density, v_d, within the BWG. This vapor-dependent term is motivated by the fact that the total path length through the BWG optics is approximately 37 meters longer than the path of the A-1 radiometer at the zenith position. There should, therefore, be a small contribution from the water vapor at ground level to the brightness temperature difference of Fig. 7. Water-vapor density is measured by the surface meteorology package at DSS 13, as plotted in Fig. 6.

Table 3 summarizes the results of a linear regression fit to the entire time series of Fig. 7, solving for the coefficients of Eq. (2) at different elevations and frequencies. The coefficients in Table 3 are unitless loss coefficients, except for c_v, which has units of loss per g/m^3.

Table 3. Coefficients for the expression of lumped-element loss in Eq. (2) that fit the brightness temperature differences in Figs. 7 and 8.

c_v, loss per g/m^3	m[a]	a_{0m}	b_{1m}	a_{1m}	b_{2m}	a_{2m}	b_{3m}	a_{3m}
				$f = 31.4$ GHz				
0.00016	1	0.02651	0.00057	−0.00006	0.00196	0.00115	−0.00035	0.00006
	2	0.02750	−0.00001	−0.00011	0.00126	0.00168	0.00019	−0.00036
	3	0.03215	0.00004	−0.00001	0.00066	0.00153	0.00060	0.00039
				$f = 22.2$ GHz				
0.00032	1	0.04776	−0.00111	−0.00088	0.00124	0.00071	0.00019	0.00029
	2	0.04866	−0.00143	−0.00042	0.00097	0.00089	−0.00012	0.00001
	3	0.05308	−0.00202	0.00026	0.00043	0.00106	0.00022	0.00012
				$f = 23.8$ GHz				
0.00027	1	0.03609	−0.00086	−0.00064	0.00158	0.00099	−0.00002	0.00022
	2	0.03710	−0.00111	−0.00034	0.00122	0.00125	−0.00008	−0.00006
	3	0.04142	−0.00154	0.00010	0.00078	0.00133	0.00028	0.00019

[a] 1 = 90 degree elevation; 2 = 45 degree elevation; and 3 = 20 degree elevation.

Of the coefficients in Table 3, the a_{0m} are the dominant terms representing the mean losses of the BWG at a given elevation. These losses vary from 3 percent to about 5 percent, depending mostly on frequency (and the related feedhorn gain). Within each frequency, the a_{0m} terms exhibit a very consistent pattern versus elevation: compared with the respective losses at 90 degree elevation ($m = 1$), the a_{0m} terms at all three frequencies increase by 0.10 percent at a 45 degree elevation angle ($m = 2$) and by 0.55 percent at 20 degree elevation ($m = 3$). As discussed later in this article, this pattern versus elevation may be related to the antenna side lobes of the DSN antenna and the fraction of such side lobes that are below the horizon at a given elevation.

Other patterns worth noting in Table 3 are as follows:

(1) Terms involving the first harmonic in azimuth (a_{1m} and b_{1m}) in Table 3 are most significant at 22.2 and 23.8 GHz, where the feedhorn gain is too low for the BWG antenna. Such errors point to an alignment eccentricity and a spillover problem within the BWG optics. The lower feedhorn gains result in wider beams within the BWG optics, which will be prone to spilling over the edges of the various reflectors, especially if the beams are not well centered. Such an enhanced sensitivity to beam alignment at the lower two frequencies is also evident in Figs. 2 and 3.

(2) The magnitudes of the second harmonics (i.e., $\sqrt{a_{2m}^2 + b_{2m}^2}$) are all between about 0.1 percent and 0.2 percent, and they increase with elevation angle and frequency. This observation can be explained, to a large part, by polarization and frequency-dependent losses in the four reflectors that steer the beam about the elevation joint of the BWG. The AWVR antenna is vertically polarized such that, in the position depicted in Fig. 1, the polarizations incident to all four reflectors are vertical. When the antenna rotates in azimuth, the polarization will also rotate with respect to these reflectors. The theoretical losses at 31.4 GHz for a polished aluminum plate at a 45 degree incidence angle are 0.053 percent and 0.106 percent for horizontal and vertical polarization, respectively. Multiplying the difference of the horizontal and vertical losses by four to represent the four reflectors yields a maximum difference of 0.212 percent that one should see as the azimuth of the BWG is rotated 90 degrees. This model accounts for about half of the magnitude of second-harmonic terms in Table 3 (i.e., the peak-to-peak change at 31.4 GHz, zenith, versus azimuth is $2 * \sqrt{b_{21}^2 + a_{21}^2} = 0.454$ percent). This result is consistent at the other frequencies (the loss difference decreases by the square root of frequency) and elevations (where the difference is diminished as one of the four reflectors tilts). Furthermore, from the known geometry of the BWG, the above model also predicts that the azimuth angles for maximum loss should be 23 degrees and 203 degrees. This is in good agreement with the phase of the zenith coefficients of Table 3, which all indicate a maxima at 30 degrees and 210 degrees of azimuth. Thus, aside from a scale factor, the second harmonic in Table 3 is consistent with the reflector loss model. Other factors—such as paint loss, surface corrosion, or surface roughness—might well account for the remaining losses.

(3) The third harmonic terms of Table 3 are the least significant (with magnitudes between about 0.01 percent and 0.07 percent) and show no apparent pattern versus frequency. Furthermore, it is difficult to imagine a simple mechanism that would impart a third-order harmonic to the excess noise of the BWG versus azimuth. At most (at 20 degree elevation and 31.4 GHz), the third harmonic translates to a standard deviation of about 0.1 K in brightness temperature. One plausible source of this error is antenna side-lobe contamination. Moreover, it is important to note that the Fourier series fit presented here incorporates—and may therefore conceal—all side-lobe contamination on spatial scales greater than 60 degrees of azimuth (where 60 degrees corresponds to the Nyquist rate in this case). The analysis presented later in this article will attempt to estimate side-lobe errors that occur on smaller spatial scales, and it will be important to bear in mind the potential level of side-lobe contamination that is suspected here on large scales.

Figure 10 gives the post-fit residual brightness temperature error given by the difference of the left and right sides of Eq. (1), or

$$D = T_{B2} - T_{B1} - L(T_S - T_{B1}) \tag{3}$$

where L is the loss estimate from Table 3 and Eq. (2), and T_S is the weighted and filtered combination of outside air and pedestal room ambient temperatures described above. The sampling interval and integration time for all three frequencies is 8.26 seconds. The theoretical noise, ΔT, for this brightness temperature measurement difference is about 0.03 K (rms), which accounts for much of the residual high frequency noise in Fig. 10.

To illustrate the significance of the vapor terms, c_v, in Table 3, Fig. 11 shows the same residuals as in Fig. 10, but with the vapor coefficient set to zero. The correlation of the excess noise in the BWG with surface humidity (Fig. 6) is evident. To confirm that these observations are truly due to humidity, Table 4 compares the vapor coefficients, c_v, of Table 3 with established water-vapor absorption models [4]. The

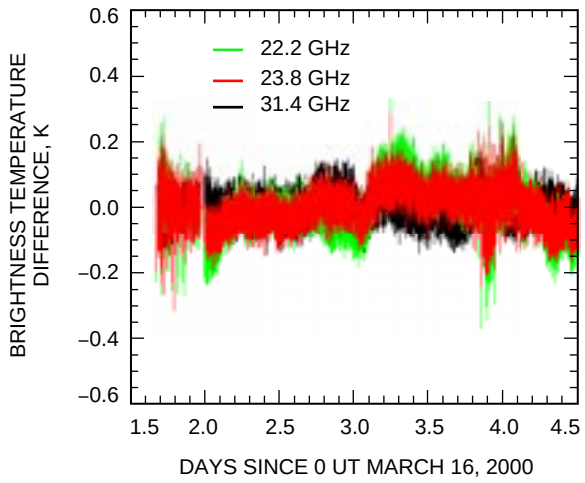

Fig. 10. A-2 — A-1 brightness-temperature residual errors from Eq. (3) after fitting constants for BWG loss and vapor sensitivity.

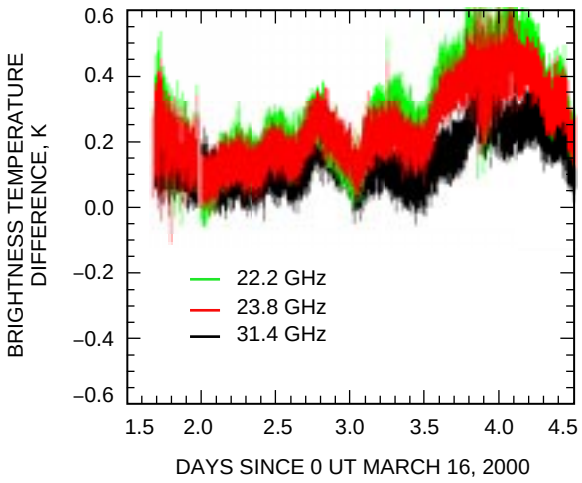

Fig. 11. The same as Fig. 10 but with no surface vapor correction (compare with vapor density in Fig. 6).

Table 4. Comparison of regression fit from Table 1 with modeled water-vapor sensitivity.

Frequency, GHz	c_v, loss per g/m^3	Derived absorption, nepers/km per g/m^3	Model, nepers/km per g/m^3
31.4	0.00016	0.00432	0.00198
22.2	0.00032	0.00865	0.00620
23.8	0.00027	0.00730	0.00541

fit parameters of Table 3 have been converted to nepers/kilometer per g/m^3 of water vapor using the estimate of 37 meters in the path-length difference of the two radiometers. A surface pressure of 850 mb, a temperature of 300 K, and an assumption of low humidity were used in the absorption model.

From Table 4, the fit coefficients derived from the present data overestimate the predicted sensitivity by about a factor of 2 at 31.4 GHz and a factor of about 1.4 in the other two channels. For the range of vapor density in the present data set—about 3 g/m^3 from day 2 to day 4 in Fig. 6—the above discrepancy at 31.4 GHz accounts for about 0.06 K of the brightness temperature change in Fig. 11. For a multi-day time series, this error could be caused by a variety of effects. For example, the 31.4 GHz calibration drift of about +1 K in 60 days (Fig. 4) can be interpolated to 0.03 K of drift from day 2 to day 4 to account for half of the above discrepancy. Correlated errors in T_S of about a 1 K to 2 K from day 2 to day 4 could also account for the above discrepancy and would be reasonable given uncertainties in the temperature estimate.

B. Examining Residual Brightness Temperature Differences with Structure Functions

To quantify the residual variations of Fig. 10, and to discriminate between errors caused by beam mismatch and antenna side lobes, the following analysis will employ temporal structure functions defined by

$$D_f(t,\tau) = \left\langle \big(f(t) - f(t+\tau)\big)^2 \right\rangle \tag{4}$$

where $<>$ is the expectation operator and f is the random process (e.g., brightness temperature or brightness temperature difference) as a function of time. For stationary random processes, the time origin, t, can be dropped so that the structure function depends only on time difference, τ.

The following analysis will also use model estimates of the water-vapor sensitivity at the observing frequencies [4] along with predicted thermal noise performance of the AWVRs, ΔT, as summarized in Table 5.

Figure 12 summarizes several structure functions derived from the 2.5 days of zenith observations following Friday, March 17. Two sets of structure functions are shown on a single scale: the curves highest on the vertical scale are the structure functions computed from the time series of zenith brightness temperature (e.g., Fig. 5), and the lower curves are structure functions of the residual (post-fit) brightness temperature difference (Fig. 10). The dashed lines in all cases are copies of the 22.2 GHz structure functions, which have been scaled to the 23.8 and 31.4 GHz frequencies using the modeled atmospheric vapor absorption sensitivities of Table 5 at the two altitudes of 890 mb (surface) and 620 mb (about

Table 5. Predicted ΔT and modeled water-vapor sensitivity for the three frequencies of the AWVRs.

Parameter	31.4 GHz	22.2 GHz	23.8 GHz
AWVR no. 1 8 second ΔT, K	0.0244	0.0221	0.0224
AWVR no. 2 8 second ΔT, K	0.0309	0.0248	0.0244
Vapor absorption, nepers/km per g/m^3			
$P = 890$ mb, $T = 300$ K (ground level)	0.00198	0.00620	0.00541
$P = 620$ mb, $T = 279$ K (3 km altitude)	0.00196	0.00838	0.00613

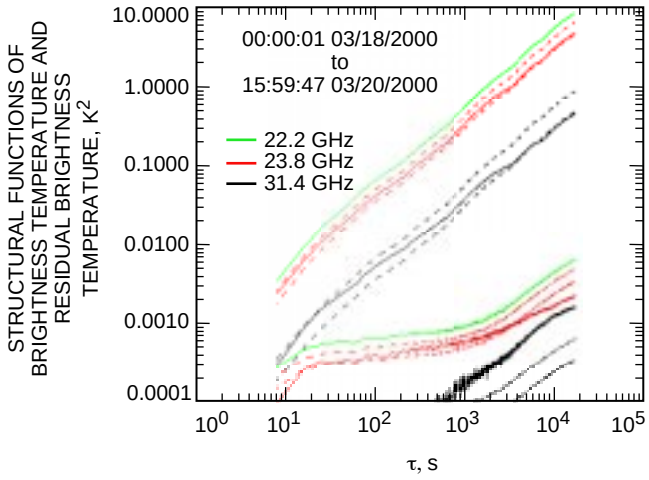

Fig. 12. Structure function of raw brightness temperatures (upper traces) from the A-1 radiometer and of the residual difference between the A-1 radiometer and the post-fit A-2 radiometer (lower traces) for the zenith data. Dashed lines represent extrapolations from the 22.2-GHz traces to 23.8 and 31.4 GHz using the vapor sensitivities from Table 3.

a 3 kilometer altitude). In all cases, an estimate of the radiometer's thermal noise (from Table 5) has been subtracted from the structure functions. The noise subtraction is only accurate to about 10 mK, so structures near or below 0.0001 K^2 tend to be inaccurate. Note that both axes of Fig. 12 are logarithmic scales.

Structure functions of total brightness temperature and of residual brightness temperature difference are plotted together in Fig. 12 so that the residuals can be judged against the actual atmospheric variability at a given time scale. The ratio of the brightness temperature structure functions to the residual structure functions provides a crude figure of merit in this respect. For example, the offset between the two solid green lines (22.2 GHz) at 100 seconds indicates that the residual structure function, at about 0.0006 K^2, is a factor of 100 less than the brightness structure function of about 0.06 K^2. In the square root, this means that the residual differences are about 10 percent of the total fluctuations at 100 second time scales. Likewise, at 1,000 and 10,000 seconds, the structure function ratios of the 22.2 GHz residuals to the brightness temperatures are about 1/600 and 1/1000, respectively, or about 4 percent and 3 percent in the square root.

The structure functions in Fig. 12 agree reasonably well with expectations. The brightness temperature structure functions increase with time, whereas the residual structure functions are relatively level from 100 to 1000 seconds. Published data [5] for water-vapor fluctuations predict a power-law versus time with an exponent that varies between 0.7 for long time scales (where the movement of the air over the antenna is large as compared with the height of the wet troposphere) and 1.7 for short time scales (where the movement is small as compared with the height). When the effects of beam averaging [3] are included, one may expect an even steeper slope with an exponent of 2 at time scales of less than 10 seconds. The time scales in these models are highly dependent on wind speeds and the spatial distribution of water vapor. The slopes of the brightness temperature structure functions in Fig. 12 exhibit an exponent near 1.5 at 10 seconds and unity from 100 to 10,000 seconds. Although the slopes do not match those in the model, the general shape of the curve, from steep to shallow with increasing time, is in agreement.

The residual structure functions of Fig. 12 (the lower curves) exhibit an initially rapid increase with time and then a flattening at 100 to 1,000 second time scales. This feature is consistent with the idea that beam offsets and mismatch errors will only increase to the point where the wind speed (typically 1 to 5 meters/second) times the time scale of interest is comparable to the spatial scale of the antenna pattern difference (in this case about 30 meters). Past 1000 seconds, the residual structure function increases again, and this feature can be attributed to slowly changing instrument errors and errors associated with the temperature correction of the BWG loss in Eq. (3).

Figure 12 also shows that the brightness temperature structure functions fit the vapor absorption model of Table 5. This is evident in the fact that the red and black lines lie between the respective dashed lines as derived from the vapor absorption coefficients and the 22.2 GHz structure function. The relative strengths of the residual structure functions past 1000 seconds, on the other hand, suggest that instrumental errors dominate past 1000 seconds, since they do not fit the vapor absorption model.

The zenith data of Fig. 12 present a best-case scenario: the antennas are at a fixed position and the line-of-sight path length through the atmosphere is as small as possible (one air-mass). When the elevation is lowered, the fluctuations in the brightness temperatures and the residuals can be expected to go up. When the antenna is in motion, one can also expect other errors, such as antenna side lobes, to corrupt performance. To examine these issues, we turn to the data of March 17. For reference, Fig. 13 gives an expanded version of Fig. 10 for the time scale of the azimuth scans. Figure 14 gives the 22.2 GHz brightness temperatures for the same period. As expected, the data of Figs. 13 and 14 clearly show the greatest brightness temperature variability in the first segment, when the elevation was 20 degrees, and the lowest variability during the middle segment, when the antennas were pointed at zenith. At 20 degrees of elevation, the path length through the atmosphere is 2.9 times larger than the path length at zenith.

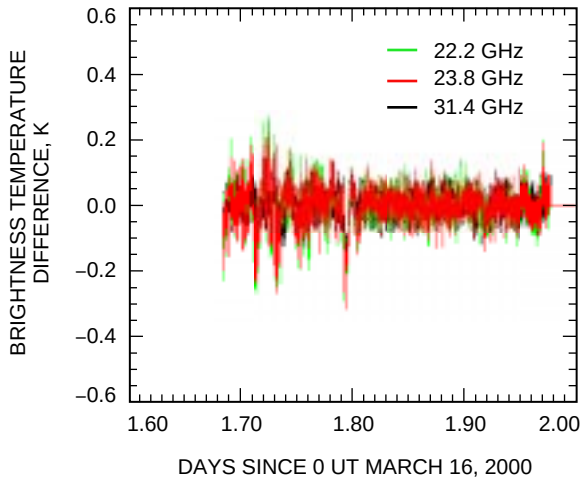

Fig. 13. Data from Fig. 10 with an expanded time scale for azimuth scans (also see Figs. 8 and 9).

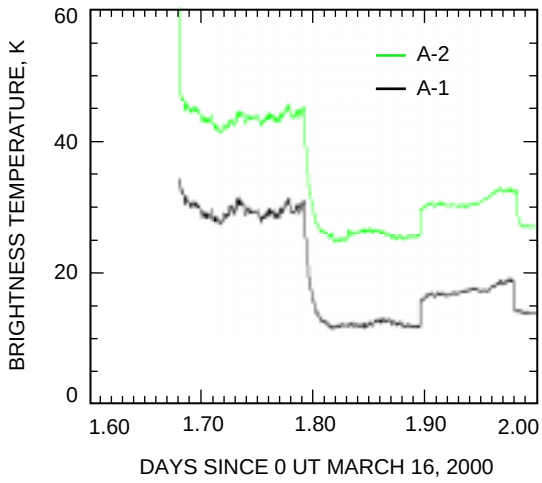

Fig. 14. 22.2 GHz brightness temperatures for the time series of Fig. 13.

To quantify the observed differences in Fig. 13, Figs. 15 and 16 give structure functions computed from data collected while the antenna was pointed at 20 degrees of elevation for two cases: stationary azimuth (Fig. 15) and scanning azimuth (Fig. 16). The stationary data were collected at 10 degrees of azimuth just before the start of the scan and at 290 degrees just after the scan. One should note that, due to the shortened experiment time as compared with the zenith data, the uncertainty of the estimated structure functions is higher and the maximum time scales are shorter. With regard to the scanning data, one should also note that the Fourier series fit of Eq. (2) and Table 3 suppresses residual differences that might exist beyond 60 degrees of azimuth motion or beyond 1200 seconds.

Comparing Fig. 15 with the zenith structure functions of Fig. 12, one clearly sees a large increase in both brightness temperature and residual brightness temperature structure functions at a 20 degree elevation angle. For example, the 22.2 GHz residual structure function at 100 seconds was 0.0006 K^2 in Fig. 12 and a factor of about 6.6 larger in Fig. 15. In the square root, this is a factor of 2.6 increase in

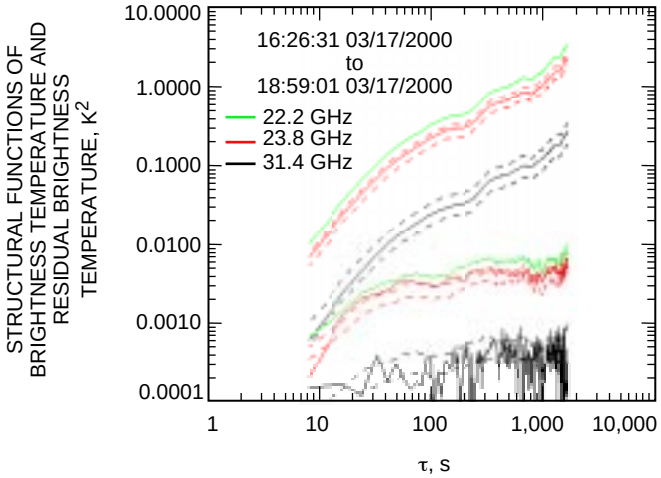

Fig. 15. Structure function of raw brightness temperatures (upper traces) of the residual (lower traces) while at 20 deg elevation and at a fixed azimuth at either 10 or 290 deg.

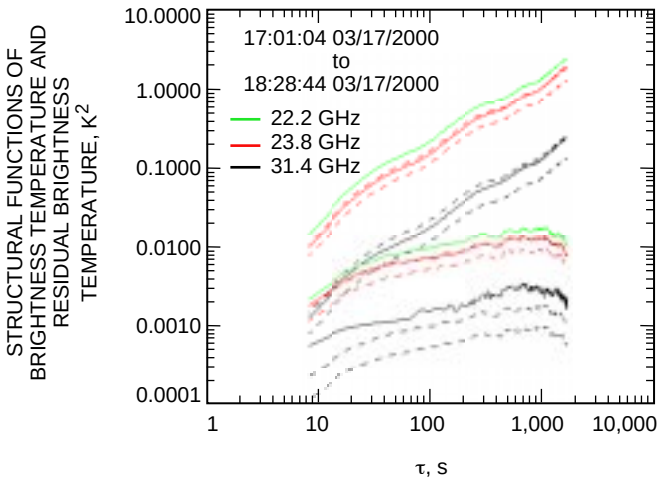

Fig. 16. Structure function while at 20 deg elevation and while azimuth scanned from 10 to 280 deg at 0.05 deg/s.

residual error, which is similar to the increase in air mass. Otherwise, the structure functions of Fig. 15 appear to scale properly with frequency and the water-vapor absorption model. The residual structures, therefore, are consistent with the effects of beam offset and mismatch.

In Fig. 16, the effects of moving the antenna in azimuth are evident. Comparison with Fig. 15 shows the residual structure functions have increased while the brightness structure functions have not increased. Also, the relative strengths among frequencies no longer match the vapor absorption model (the black line does not fall between the dashed lines). Thus, there appears to be an additional component in the residuals that does not originate in the water-vapor variability of the atmosphere.

C. Analysis of the Excess Noise During BWG Motion

Some of the additional noise in Fig. 16 is believed to be contamination from side lobes of the BWG antenna near or below the horizon. The hillside and terrain surrounding the pedestal at DSS 13 present a spatially uneven brightness temperature to these side lobes, so antenna motion should result in antenna noise temperature fluctuations. To a first order, the magnitudes of the side lobes are proportional to the cross-sectional area of the BWG subreflector and supporting quadripod structure, which is independent of the radio frequency. One may therefore anticipate that the side-lobe contribution to the residual structure functions of Fig. 16 should be equal at the three frequencies. With this assumption, it is possible to solve for and separate the side-lobe errors using the vapor absorption coefficients of Table 5. Given three brightness temperatures, a solution can be formulated for three unknown parameters of a frequency-independent structure function, a water-vapor structure function, and a weighting factor for the two altitudes of Table 5. The details of this solution will be omitted here for brevity, but Figs. 17 and 18 give the results when the solution is applied to the structure functions of Fig. 16. Figure 17 gives the structure function of the additive noise (blue) along with the structure functions from Fig. 16 after subtracting the additive noise. The mixing parameter, plotted in Fig. 18, is predominantly greater than 70 percent, which means that the effective altitude for water-vapor fluctuations is closer to the ground than the 3 kilometer altitude.

If the assumption of frequency independence in the side-lobe contamination is correct, and if no other errors have been neglected, then Fig. 17 should be a reasonable representation of side-lobe contamination (blue curve) in the context of beam offset and mismatch errors (black, red, and green curves) at a 20 degree elevation angle. Figure 17 represents just one sample case, however, and the results will vary with different atmospheric conditions. Also, models show that at low elevation angles the beam offset

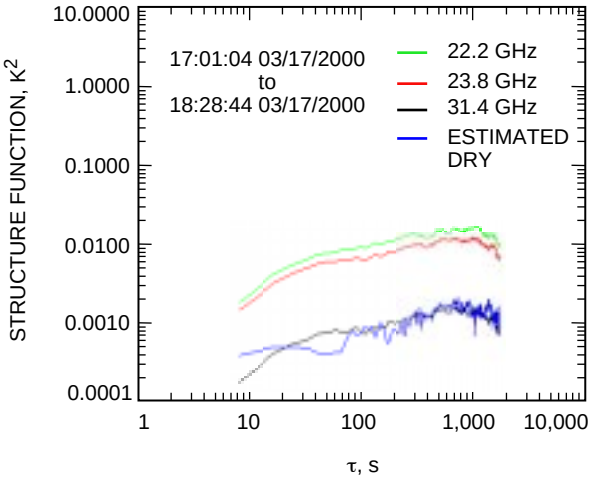

Fig. 17. Structure function of post-fit residuals from Fig. 16 after subtracting an estimate for an additive structure function (blue trace) of equal magnitude from all three frequencies.

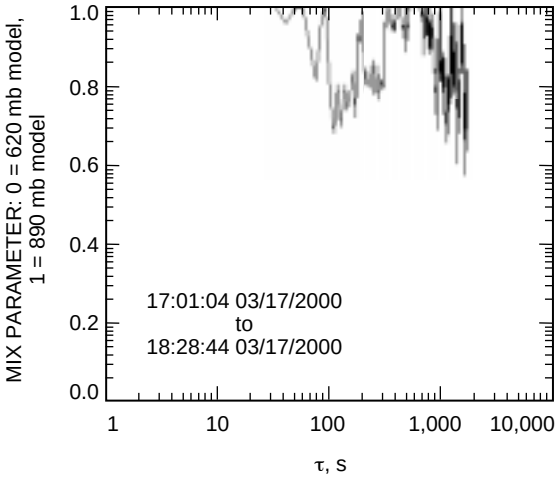

Fig. 18. Retrieved mixing parameter for Fig. 16: mix parameter of 1 means the 890 mb vapor model of Table 5 applies; 0 means the 620 mb model applies; intermediate values represent an interpolation.

effect depends strongly on wind direction and on the azimuth difference between the pointing direction and the antenna separation [7]. Such a dependence may explain why the residual structure functions of Fig. 17, after subtracting the estimate of side-lobe contamination, are still about 2 to 3 times higher than those of Fig. 16 when the antenna was stationary at 10 and 290 degrees of azimuth.

To support the above observations, Fig. 19 gives the structure functions derived from a different data set (March 10) at the same 20 degree elevation angle as Figs. 15 through 17, but with a fixed azimuth of 180 degrees (south). In Fig. 19, the residual structure functions—and the ratio of the residual to total brightness temperature structure functions—are closer to those of the scanning data in Fig. 17 than they are to the stationary data of Fig. 15. Another data set (not plotted here) from March 9 with the same observation angles yields the same result. Therefore, the residual noise while scanning the antenna (Fig. 17) is not abnormally high when compared with other data at a southern azimuth.

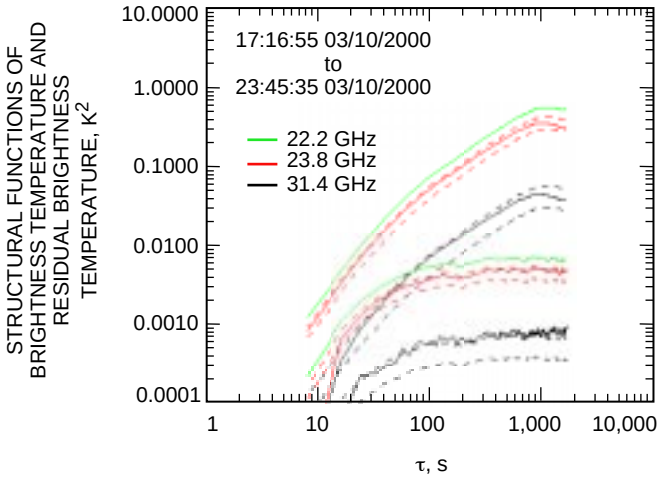

Fig. 19. Structure functions for March 10, 2000, data in which azimuth is 180 deg and elevation is 20 deg.

Figures 20 and 21 give the structure functions derived from data collected on March 16 while the antenna was at an elevation of 20 degrees and either fixed (Fig. 20) or scanning in azimuth (Fig. 21). Figures 20 and 21 are directly comparable to Figs. 15 and 16 as they are derived from almost identical observation strategies (with only minor differences in the rate and extent of the azimuth scan). The most important difference to note is that the atmosphere was much "quieter" on March 16 than on March 17, as is evident in the lower structure functions for the total brightness temperatures. In Fig. 21, the residual structure functions clearly do not scale with frequency in a way consistent with the water-vapor absorption model. The structure functions in all three frequencies are approximately 0.001 K^2 near 100 to 1,000 seconds, suggesting that the residuals are dominated by the same additive component that was estimated in Fig. 17. The persistence of this error under different atmospheric conditions—together with the fact that this error only appears while scanning the antenna and the fact that this error appears in approximately equal magnitudes at all three frequencies—implicates side-lobe contamination

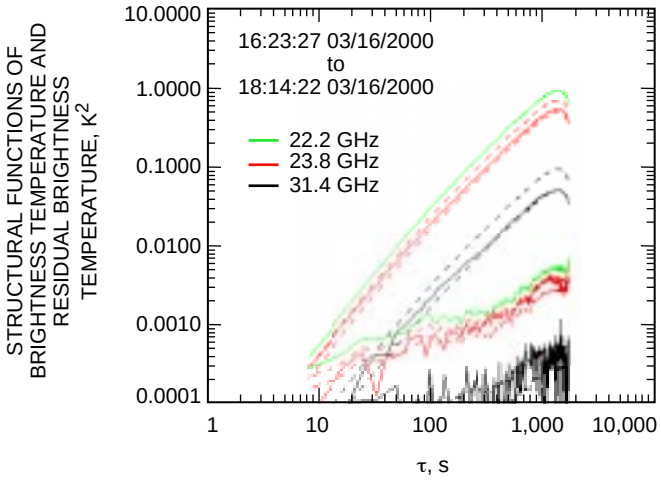

Fig. 20. Structure functions of data collected on March 16, 2000, with 20 deg elevation and azimuth fixed at 10 and 290 deg.

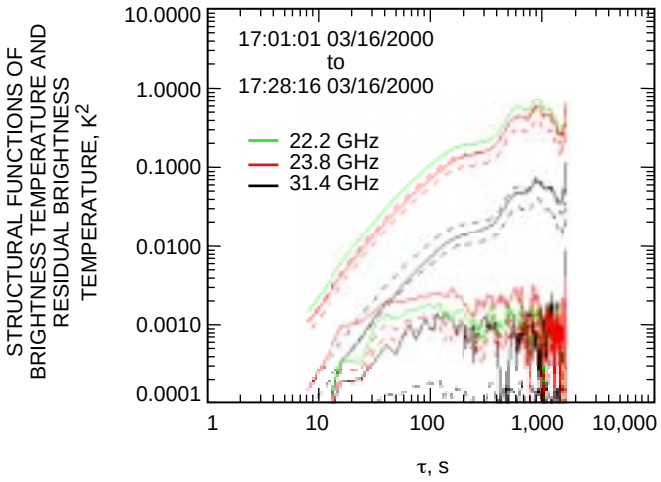

Fig. 21. Structure while scanning azimuth at 20 deg elevation; only a partial scan from 10 to 180 deg in azimuth was completed.

as the source. The structure functions of Figs. 17 and 19 both suggest that this side-lobe contamination contributes about 0.03 K (= square root of 0.001 K^2) of uncertainty to the system noise temperature at approximately 50 to 500 second time scales, or through about 2.5 to 25 degrees of azimuth motion given the scan rates of the experiment.

D. Results at 45 and 90 Degree Elevation Angles: Fixed Position and Scanning Azimuth

Again as regards the March 17 data, Figs. 22 and 23 provide structure function comparisons for the data collected at 45 degrees of elevation. As with the 20 degree elevation plots, these structure functions are plotted from data collected with and without the antenna scanning. At 45 degrees of elevation, while at a fixed azimuth (Fig. 22) or scanning (Fig. 23), the residual structure functions and the brightness temperature structure functions evidently fit the absorption model. Therefore, there is no evidence of the additive noise (from side lobes) that was observed at 20 degrees while scanning. Comparing fixed versus scanning, there is again an increase in the residual structure functions as the antenna moves in

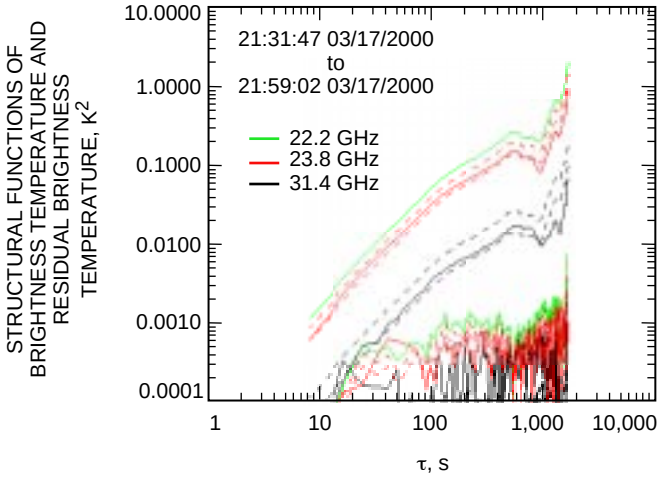

Fig. 22. Structure functions for data collected at a fixed azimuth and at 45 deg elevation.

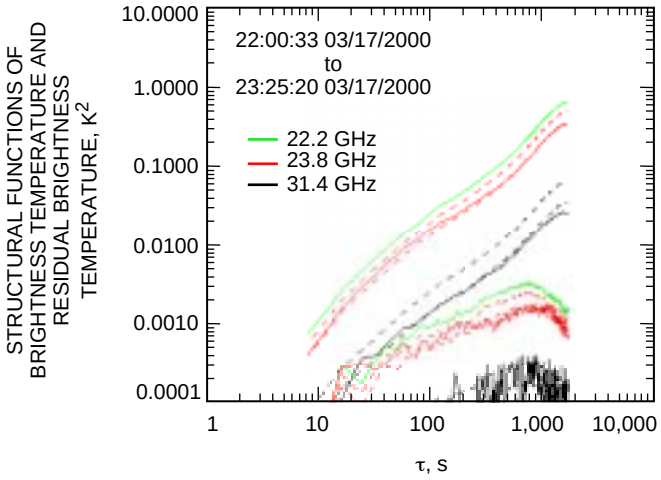

Fig. 23. Structure functions for data collected while scanning azimuth and holding elevation at 45 deg.

azimuth, but the difference is less pronounced than at the 20 degree elevation angle. The ratios of residual to brightness structures at 100 seconds are about 1/60 while fixed and 1/40 while scanning, or about 13 percent and 16 percent in the respective square roots. As in the 20 degree elevation case, the improved performance at the fixed azimuths of 10 and 290 degrees may be related to a favorable beam offset as compared with positions toward the south.

For 90 degrees of elevation, Figs. 24 and 25 present again structures while fixed and while scanning. The structures again appear to fit the absorption model with one exception: in Fig. 25 the 23.8 GHz residual structure exceeds the 22.2 GHz residual while scanning the antenna in azimuth. Due to the lack of more zenith data while scanning azimuth, there is no good explanation for this anomaly. This anomaly is a constant over the entire time scale from 10 to 1000 seconds, which leads one to suspect that a few transients in the 23.8 GHz channel could explain the discrepancy. In any case, the error is very small, at about 20 mK. Otherwise, there is no significant increase in the residual errors when the antenna is

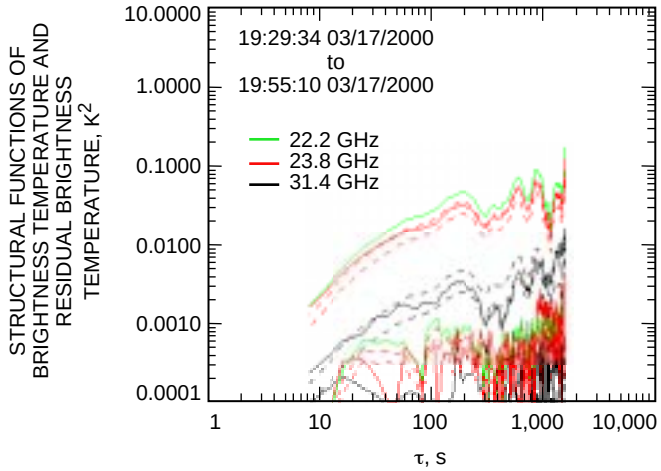

Fig. 24. Structure functions for data collected at a fixed azimuth and 90 deg elevation.

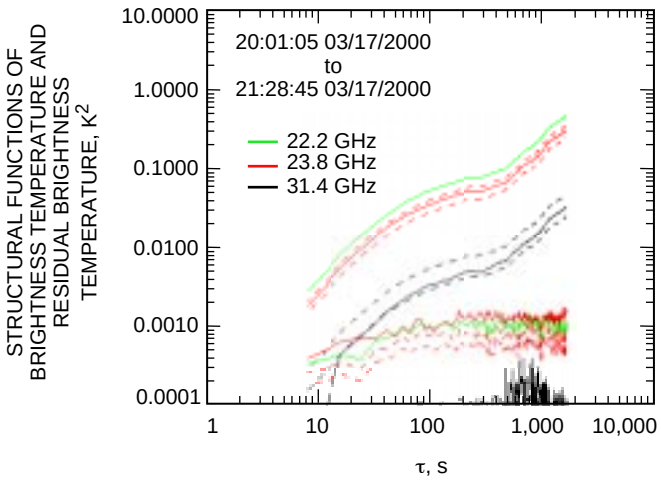

Fig. 25. Structure functions for data collected while scanning azimuth and holding elevation at 90 deg (zenith).

scanned—which is a departure from the 20 and 45 degree cases. Based on the 22.2 GHz data, the ratios of residual to brightness structures at 100 seconds in Figs. 24 and 25 are both about 1/50, or about 14 percent in the square root.

The decreased side-lobe contamination observed in the residual structure functions at these higher elevation angles, as compared with the 20 degree elevation case, is consistent with the patterns noted with the average loss coefficient (a_{0m}) and with the third-harmonic terms of Table 3 (a_{3m} and b_{3m}). In all cases, the 20 degree elevation angle data reveal the highest side-lobe contamination. This pattern is summarized in Table 6. Table 6 provides estimates of the side-lobe contamination versus scale of azimuth motion at the different elevation angles. The second column (small scale) was estimated from structure functions such as Fig. 17. The third column (60 degree scale) was estimated with third-harmonic fit coefficients of Table 3. The fourth column (360 degree) shows the average contribution over all azimuth angles; T_N is defined here as the total side-lobe contribution at zenith (which is unknown), and the increases at 45 and 20 degree elevations were estimated from corresponding changes of the a_{0m} coefficients of Table 3 versus elevation.

Table 6. Estimates of BWG side-lobe contribution to noise temperature at various elevation angles and scales of azimuth motion.

Elevation	0.5–25 deg azimuth motion	∼60 deg azimuth motion	360 deg azimuth average
20 deg	0.03 K	0.1 K	$T_N + 1.6$ K
45 deg	<0.01 K	0.05 K	$T_N + 0.3$ K
90 deg	<0.01 K	0.05 K	T_N by definition

E. Sidereal Tracking

The final data set to be presented in this article is of the sidereal track on March 24. This scan is important because it involves movement in elevation as well as azimuth. The scan rate of these data, at about 4 millidegrees/second, is 12 times slower than the azimuth scans of March 17. Figures 26 and 27 give the raw brightness temperature at 22.2 GHz and the elevation angle for this experiment, which lasted approximately 4.5 hours. Figures 28 and 29 give the post-fit residuals and the structure functions of the post-fit residuals for the same time span. The 23.8 GHz data are missing in these plots as there was a strong radio interference problem on this day from other equipment in the pedestal room at DSS 13. The post-fit residuals of Fig. 28 are based on a fit to the BWG loss expression of Eq. (2), except that the series was truncated at $n = 2$ and a single term proportional to the sine of the elevation angle was added. Again, these are ad hoc fits that will suppress errors on the largest angular scales (>60 degrees).

The time series of brightness temperature in Fig. 26, and of the residuals in Fig. 29, show the increased atmospheric noise at lower elevations. The dependence of the structure functions on frequency confirm that most of the residual errors originate in atmospheric water vapor. Only a very slight side-lobe contribution to the 31.4 GHz residual structure of about 0.0001 K^2, or 0.01 K in the square root, is evident in Fig. 29 (where the residual black line is just above the dashed lines). Considering the fraction of the data collected at low elevation, this 0.0001 K^2 excess error is reasonably consistent with the 0.001 K^2 errors observed at 20 degree elevation.

The structure function of the raw brightness temperature at 31.4 GHz also exceeds the scaled 22.2 GHz value at the longer time scales in Fig. 29. Such an error can be anticipated since the increase of air mass with lower elevation will add a “dry” atmospheric component that originates in other gases, such as oxygen.

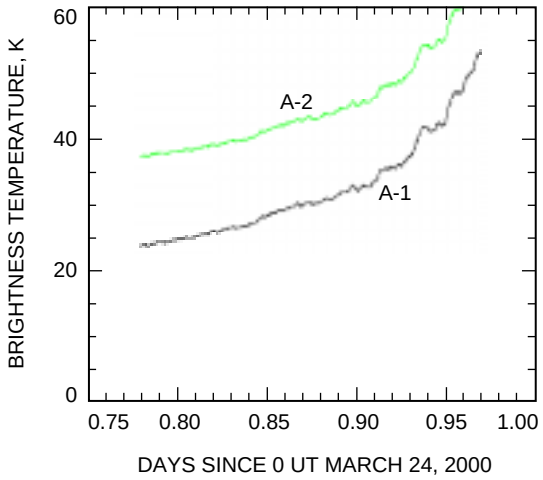

Fig. 26. 22.2 GHz brightness during sidereal track.

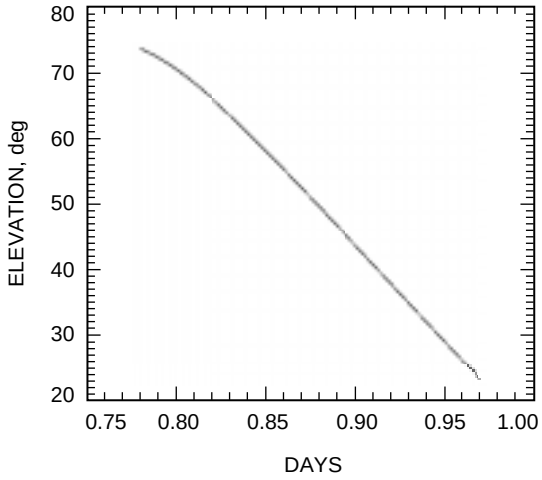

Fig. 27. Elevation angle during sidereal track.

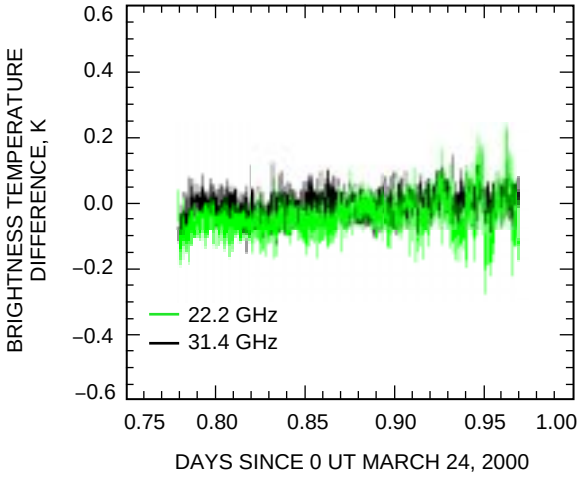

Fig. 28. Post-fit residual error during sidereal track; 23.8 GHz data were corrupted in the BWG by RFI and have been omitted from the figure.

From the 22.2 GHz data of Fig. 29, the ratio of the residual structure to the brightness structure at 100 seconds is about 1/70, or about 12 percent in the square root. This ratio is again consistent with errors presumed to be caused by beam mismatch and offset.

V. Conclusions

The difference between the atmospheric water-vapor fluctuations seen with the BWG radiometer and the external radiometer range from 10 percent to 26 percent of the total fluctuation level at 100 second time scales. The fractional difference decreases toward longer time scales. The magnitudes of these differences, plus their dependence on the time scale, frequency, and elevation angle, suggest that they are due to the different volumes of air sampled by the two radiometers (the beam offset and beam mismatch).

By embedding a radiometer into a BWG antenna, the calibration performance could be improved at 100 second time scales, perhaps to below the Cassini requirements. For time scales shorter than

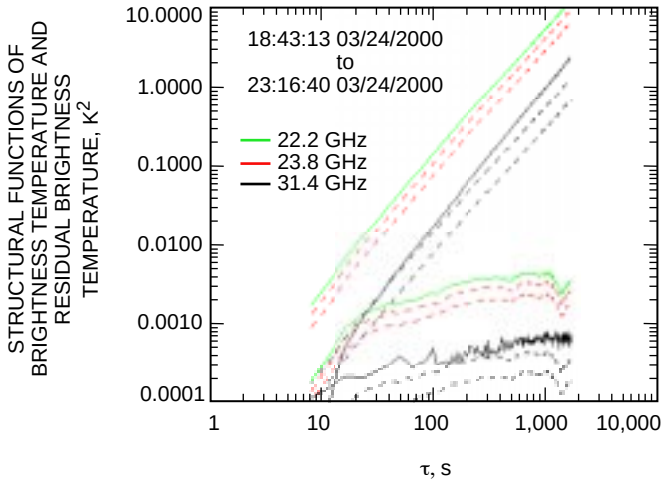

Fig. 29. Structure functions for data collected during sidereal track.

100 seconds, the beam-offset and mismatch errors are so large that an embedded location would be required for useful calibration. Below 20 to 30 second time scales, even an embedded location is insufficient unless the thermal radiometer noise can be reduced by use of a cryogenic receiver.

The noise temperature of the beam-waveguide optics appears to be well behaved; a three-term Fourier series expansion provides a good fit to the observed BWG electrical losses versus azimuth. For spatial scales of about 0.5 to 25 degrees (or 10 to 500 seconds at the 0.05 degree/second scan rate of these experiments), such a model fits the data to an accuracy better than 0.01 K of noise temperature at elevation angles of 45 degrees or higher. Suspected antenna side-lobe contamination of about 0.03 K in rms brightness temperature appears at the lowest elevation angle of 20 degrees. This is smaller than the beam-offset and mismatch error for an external radiometer. The performance of the BWG is therefore adequate for measuring water-vapor fluctuations to a higher precision than the existing (external) AWVR system can provide on 100 second time scales. On larger spatial scales, the side-lobe contamination appears to be greater. For time scales longer than 1,000 seconds, the external radiometer will give superior calibration performance.

Our results indicate that there would be considerable utility in a cryogenically cooled embedded radiometer in applications requiring atmospheric calibrations at sub-100 second time scales. Most science applications involve sidereal tracking at a rate of 0.004 degrees/second, or 0.4 degrees in 100 seconds, in which case antenna side-lobe contamination will most likely fall below 0.01 K of noise temperature. Given this lower bound, and given the combined thermal noise and beam mismatch of 0.04 to 0.08 K in the AWVR, these observations show that a factor of 4 to 8 improvement over the AWVR is possible. Such a capability would meet Cassini requirements at 100 second time scales.

Acknowledgments

The author thanks the staff at DSS 13 and Goldstone, including Bob Rees, Lester Smith, and Richard Thomas.

References

[1] G. M. Resch, Y. Bar-Sever, S. J. Keihm, P. Kroger, R. P. Linfield, M. J. Mahoney, A. Tanner, and L. P. Teitelbaum, "Atmospheric Calibration for Precision Doppler Tracking of Spacecraft," *Planetary Space Science*, vol. 46, no. 9/10, pp. 1257–1261, 1998.

[2] A. B. Tanner, "Development of a High Stability Water Vapor Radiometer," *Radio Science*, vol. 33, no. 2, pp. 449–462, March–April 1998.

[3] R. P. Linfield, "Effect of Aperture Averaging Upon Tropospheric Phase Fluctuations Seen With a Radio Antenna," *Radio Science*, vol. 33, no. 5, pp. 1353–1359, September–October 1998.

[4] S. L. Cruz Pol, C. S. Ruf, and S. J. Keihm, "Improved 20- to 30-GHz Atmospheric Absorption Model," *Radio Science*, vol. 33, no. 5, pp. 1319–1333, September–October 1998.

[5] R. N. Treuhaft and G. E. Lanyi, "The Effect of the Dynamic Wet Troposphere on Radio Interferometric Measurements," *Radio Science*, vol. 22, no. 2, pp. 251–265, March–April 1987.

[6] G. Elgered, "Tropospheric Radio Path Delay From Ground-Based Microwave Radiometry," Chapter 5, *Atmospheric Remote Sensing by Microwave Radiometry*, edited by M. Janssen, New York: Wiley, pp. 215–258, 1993.

[7] R. P. Linfield and J. Z. Wilcox, "Radio Metric Errors Due to Mismatch and Offset Between a DSN Antenna Beam and the Beam of a Troposphere Calibration Instrument," *The Telecommunications and Data Acquisition Progress Report 42-114, April–June 1993*, Jet Propulsion Laboratory, Pasadena, California, pp. 1–13, August 15, 1993.
http://tmo.jpl.nasa.gov/tmo/progress_report/42-114/114A.pdf